


RESEARCH ARTICLE OPEN ACCESS

Simulation of Autogenous Self-Healing in Lime-Based Mortars

Cristina De Nardi  | Sina Sayadi | Iulia Mihai | Anthony Jefferson

Resilient Structures and Construction Materials (RESCOM) Research Group, School of Engineering, Cardiff University, Cardiff, Wales, UK

Correspondence: Cristina De Nardi (denardic@cardiff.ac.uk)

Received: 6 May 2024 | **Revised:** 3 September 2024 | **Accepted:** 4 October 2024

Funding: This study was funded by Leverhulme Trust ECF-2022-235; Engineering and Physical Sciences Research Council EP/P02081X/1; HORIZON EUROPE Marie Skłodowska-Curie Actions 860006; SMARTINCS PROJECT; and European Cooperation in Science and Technology CA15202.

Keywords: built heritage | lime-based mortars | self-healing modelling

ABSTRACT

Throughout history, architectural heritage has been constructed using masonry, clay or stone elements, and lime-based mortars. Over time, old buildings are subjected to different degrees of movement and degradation, leading to the formation of microcracks. Water dissolves and transports lime in mortar, but when the water evaporates, the lime is deposited and heals cracks in a process known as autogenous healing. Lime-based mortars can regain some mechanical properties due to their healing capacity, given certain conditions. In the present work, a constitutive formulation has been developed to simulate cracking and healing in lime-based mortars. The proposed model captures the residual displacements within cracks, associated with interacting crack surface asperities, as well as the healing effect on mechanical properties. A new approach is described which expresses these mechanisms mathematically within a micromechanical formulation. The proposed model was validated by comparing the outputs with experimental data. The results show that the new continuum micromechanical damage-healing model could capture the damage-healing cycle with good accuracy.

1 | Introduction

A sense of place, identity and aesthetical well-being are fostered by cultural assets such as historical buildings, archaeological sites and monuments [1]. The current generation has a duty to future generations to maintain heritage structures.

Architectural heritage worldwide predominantly comprises masonry units and mortar. These components exhibit distinct mechanical properties and geometries, and their arrangement can vary, resulting in different types of masonry assemblages [2, 3].

Given their important role for economies and societies, the assessment, preventive conservation and maintenance of historical masonry structures remain key focusses of political strategy in both the UK and Europe [4, 5]. It is widely acknowledged that preventive measures are far more cost-effective than repairing damage. Such damage to historic structures often results in the loss of both buildings and artworks, leading to: (i) a tangible loss of artistic and historical materials, and (ii) an intangible loss of memory and cultural identity for the people to whom that legacy belongs [6].

In the past, historic building as well as landscapes have experienced and survived significant climatic events, thus

This is an open access article under the terms of the [Creative Commons Attribution](https://creativecommons.org/licenses/by/4.0/) License, which permits use, distribution and reproduction in any medium, provided the original work is properly cited.

© 2024 The Author(s). *International Journal for Numerical and Analytical Methods in Geomechanics* published by John Wiley & Sons Ltd.

demonstrating some resilience with respect to earthquakes, accidents, cycles of moisture wetting and drying and freezing [7].

This longevity might - in part - be explained by the well-known self-healing abilities of lime-based mortars. The autogenous self-healing behaviour of mortars with a high lime content was first studied by Anderegg [8], in 1942, who discovered that atmospheric water, once percolated into the matrix, can dissolve the calcite in the binder. Saturated water can migrate to cracking zones and eventually reprecipitate calcite and other minerals, promoting the healing through crystal deposition in microcracks. The presence of water is then one of the main factors coupled with the degree of carbonation. As underlined by Lubelli et al. [9] the carbonation reaction proceeds from the surface, which is in contact with the air, to the inner part of the mortar progressively. Not-fully carbonated particles can be dissolved and subsequently transported and reprecipitated elsewhere. Moreover, the presence of impurities, such as $\text{Na}(\text{OH})$ and Na_2CO_3 , might increase the calcite solubility and thus enhance the healing phenomena [10].

Recent studies have focussed on the effect of self-healing on the mechanical performance of natural hydraulic lime (NHL) mortars [11]. These have shown that, depending on the age of precracking and the level of damage, the strength increases by between 40% and 20%, with higher increases being associated with earlier age precracking.

In the context of this study, an analysis of lime mortar as an individual material is carried out, encompassing both its experimental and modelling aspects as documented in the existing literature. Subsequently, attention is directed towards its role within a masonry system, where the implications of these findings are expounded upon.

Compared to cement mortar, there is a scarcity of literature regarding the mechanical properties of hydraulic lime-based mortars [2, 3]. Previous studies have highlighted a knowledge gap in our understanding of this material [12–14]. Despite a significant amount of experimentation aimed at designing new mortar compositions and understanding its behaviour, there has been little focus on developing a comprehensive model to fully represent the stress–strain response of lime-based mortars when subjected to compression, which is a critical factor in masonry structures. According to Tassios [15], lime-based mortars exhibit greater strength under compression than tension, with the uniaxial compressive strength being approximately 10 times greater than the uniaxial tensile strength. Using the EulerBernoulli and Timoshenko models as a basis, Grazzini et al. [16] formulated a bi-modulus model to analyse the results of three and four-point bend tests performed on NHL samples. The findings showed that the model was more effective in accurately representing the experimental data in the four-point bend tests compared to tensile tests. Diogo and Figueiredo [17] have demonstrated the validity of a model to predict the compression strength peak of lime mortars, based on the chemical and physical properties of the binder, water/binder and binder/aggregate ratio. Compressive strength differences between measured and predicted values range between 39% and 4%, with older samples showing the best agreement.

Modelling strategy for masonry structures

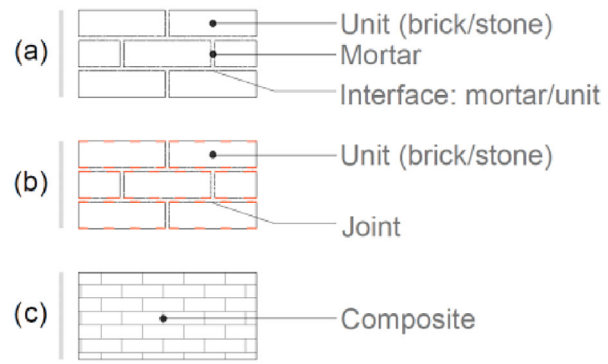


FIGURE 1 | Modelling approaches for masonry structures: (a) detailed micromodelling, (b) simplified micromodelling and (c) macromodelling.

The crucial contribution of mortar joints to the load-bearing capacity of masonry structures is well-recognised [2, 3]. The quality and the thickness of these joints are considered the most significant parameters influencing the mechanical behaviour of the masonry [18] since the majority of the deformations and movements occur in mortar layers [19, 20]. More recently, the influence of the healing capacity of lime-based mortars was studied by De Nardi et al. [21]. The authors tested masonry triplets in shear with and without lateral precompression. The findings of this study indicate that autogenous healing leads to a slight increase in the cohesion value, while significantly and positively affecting the friction coefficient, resulting in a doubling of its value [22].

Masonry is generally considered an anisotropic heterogeneous material, and analysing, understanding and capturing its structural behaviour is challenging. For nonstandard masonry, such as historical masonry, recourse to numerical modelling is often required to understand the structural behaviour under various loading conditions [3, 23, 24]. Several investigations have highlighted the need for viable and accurate methods for analysing historical masonry structures [19, 25–29].

The main modelling strategies for masonry are summarised in three main groups, listed in descending order of refinement [30, 31]

- detailed micromodelling where units and mortar in the joints are represented by continuum elements, while the unit-mortar interface is depicted by discontinuous elements (Figure 1a);
- simplified micromodelling, where bricks units are represented as continuum elements, and the behaviour of the mortar joints and unit-mortar interface is modelled into discontinuous brick/brick interface elements (Figure 1b);
- macromodelling (one-phase material). Units, mortar and unit-mortar interfaces are smeared out in a homogeneous continuum (Figure 1c).

The detailed micromodelling approach offers high accuracy in results, but its computational demands limit the size of the

numerical models. In this method, units and mortar joints in masonry are considered separately, each governed by distinct constitutive laws. Mechanical properties are derived from experimental tests on individual components [32–35].

Simplified micromodelling (two-phase material) involves representing expanded units with continuum elements, while the behaviour of mortar joints and unit-mortar interfaces is combined into discontinuous elements that act as zero-thickness interfaces [36–39].

Simplified micromodelling and macromodelling are generally preferred because they enable the structural analysis of larger models. The main advantages of using homogenisation techniques are that once the properties of the components are fully known, the behaviour of masonry - considered as a composite material - can be accurately predicted without the need for extensive experimental tests. Changes in geometry, such as unit size, joint thickness or geometrical arrangements, can be analysed through numerical modelling [40–44].

There is a substantial amount of information available regarding the mechanical properties and behaviour of cement mortar masonry. However, there is a noticeable lack of literature concerning the performance of lime-mortar masonry [45, 46]. Although it is possible to measure masonry compressive strength and other mechanical properties through experimental laboratory tests, these tests require significant resources in terms of materials and efforts.

The use of computational tools is essential in order to accurately represent the mechanical properties of a structure, assess its current condition, identify the causes of damage, determine the structural strength under various loading conditions and ultimately design appropriate remedial measures. Considering this, it is crucial to simulate the time-dependent mechanical behaviour of masonry components, taking into account their irreversible degradation due to mechanical loads or their ability to heal through self-healing processes.

Given the increasing effects of climate change, which exposes our built heritage to more extreme hazards, understanding the behaviour of lime mortar under various loads and environmental conditions, as well as its long-term evolution, is crucial. It has been proven that the strength of lime mortars increases over time. In experiments, the strength increase ranged from 40% to 25% [11], relative to precracking levels. The degree of strength gain depended on the age of precracking, with the greatest strength increases measured in specimens which were cracked at an early age. In the present work, an advanced micromechanical model is proposed to represent microcracks and self-healing behaviour in lime-based mortars. This model builds on an existing two-phase composite micromechanical constitutive model for concrete, which accounts for anisotropic microcracking [44, 47, 48]. A number of fundamental changes were necessary to the microlevel constitutive relationship to make the model applicable to lime mortar since this material has very different characteristics from those of concrete. The calibration process was undertaken using experimental data on the mechanical performance of NHL samples under compression.

Cube specimens were precracked at different ages and levels of damage and then cured in water to evaluate healing efficacy. Model parameters were refined based on the results from one healing cycle and validated against additional data to ensure accuracy and reliability. The study concludes with findings derived from these validations.

The paper is structured as follows:

- Section 2 presents the model theory and describes the numerical implementation of the model.
- Section 3 reports a series of mechanical responses for specimens with different ages, damage levels and degrees of healing. The data were obtained by the authors at the University IUAV of Venice.
- Section 4 presents a series of validations that involve both damage and healing behaviour.
- Section 5 draws some overall conclusions from the study.

2 | Micromechanical Approach

2.1 | A Review of the Main Modelling Approaches

The mechanical characteristics of lime-based mortar closely resemble those of low-strength concrete. As such, this study first evaluated and adapted established models, initially developed for concrete, to effectively model the behaviour of lime-based mortar using experimental data. The following models were considered: (i) Desayi and Krishnan [49]; (ii) Saenz [50]; (iii) Popovics [51]; (iv) Carreira and Chu [52] and (v) fib Model Code 2010 [53].

2.2 | Homogenised Properties

Experimental observations indicate that lime mortars have a multiphase structure with complex nonlinear behaviour. Using a micromechanical formulation can provide an accurate tool for linking these phases and deriving an overall constitutive equation to simulate the mechanical properties of this type of material. Effective compliance tensors of composite materials for a dilute case with a volume fraction of inclusion less than 0.1 where the inclusion interaction is negligible, can be calculated using the Eshelbian method [54]. For lime mortar, for which the volume fraction of inclusion phases is more than 5%, homogenisation estimation techniques are required. For composite materials with matrix-inclusion structures like mortar and aggregate, the Mori–Tanaka homogenisation technique [55] is recommended [56]. The effective stiffness matrix is used in a constitutive equation to relate the far field strain ($\bar{\epsilon}$) to the far-field stress ($\bar{\sigma}$):

$$\bar{\sigma} = \mathbf{D}_{\text{eff}} \bar{\epsilon} \quad (1)$$

where the homogenised stress–strain constitutive tensor, derived using the Mori–Tanaka method, is as follows:

$$\mathbf{D}_{\text{eff}} = \mathbf{D}_m + (f_\Omega (\mathbf{D}_\Omega - \mathbf{D}_m) \mathbf{A}^{\text{dill}}) (f_m \mathbf{I} + f_\Omega \mathbf{A}^{\text{dill}})^{-1} \quad (2)$$

where \mathbf{D}_{eff} , \mathbf{D}_m , \mathbf{D}_Ω , f_Ω and f_m are equivalent composite stiffness, matrix stiffness, inclusion stiffness, inclusion and matrix volume fraction, respectively. In this equation, \mathbf{A}^{dill} and \mathbf{I} are the dilute strain concentration and identity matrix, respectively. The strain concentration tensor for a two-phase matrix inclusion system is given by:

$$\mathbf{A}^{\text{dill}} = (\mathbf{I} + \mathbf{S}\mathbf{C}_m(\mathbf{D}_\Omega - \mathbf{D}_m))^{-1} \quad (3)$$

where \mathbf{I} is identity matrix, \mathbf{S} is the Eshelby tensor and \mathbf{C}_m is matrix elastic compliance tensor.

2.3 | Microcracking and Residual Displacement

The particular novelty in the micromechanical model lies in the way that a permanent ‘wedging strain’ tensor has been incorporated into the model. This strain permanent strain component is necessary to represent the significant permanent displacements that are exhibited by mortar when it is subjected to cyclic loading. This new strain component is in addition to the existing inelastic healing and damage strain tensors. The wedging strain is associated with small particles becoming lodged in microcracks and the interaction of opposing rough microcrack surfaces, which prevent microcracks from fully closing. The incorporation of the new terms into the constitutive relationship (15) was far from trivial, and developing a robust algorithm for the evolution of the multiple nonlinear processes, in a way that satisfied the second law of thermodynamics, was challenging.

Furthermore, it was necessary to calibrate all the damage and healing evolution functions for a different material, specifically lime-based mortar, rather than the usual concrete. As a result, the model had to undergo validation and be applied to lime mortar for the first time.

This marked the first time a model was employed to simulate the mechanical properties of lime-based mortars, capturing their unique behaviour, including their self-healing capabilities, which set them apart from traditional concrete.

2.3.1 | Basic Theory

Smeared crack approaches can model the constitutive behaviour of quasi-brittle materials. The direct method of micromechanics formulation is used in this paper to calculate the additional strain caused by microcracking process as well as its effect on overall stiffness matrix. This formulation can simulate the anisotropy caused by microcrack evolution [57]. Accounting the additional microcracking strain gives the following constitutive equation:

$$\boldsymbol{\sigma} = \mathbf{D}_{\text{eff}} (\boldsymbol{\varepsilon} - \boldsymbol{\varepsilon}_{\text{add}}) \quad (4)$$

where $\boldsymbol{\varepsilon}_{\text{add}}$ is the total additional microcracking strain (in Voigt notation), calculated by integrating the contributions from the additional strain on all crack planes.

For a single crack plane, the additional strain is calculated by [58] methods.

$$\boldsymbol{\varepsilon}_\alpha = f \frac{16(1 - \nu_m^2)}{3E_m} \begin{bmatrix} \mathbf{s}_{rr} \\ \frac{4}{2-\nu_m} \mathbf{s}_{rs} \\ \frac{4}{2-\nu_m} \mathbf{s}_{rt} \end{bmatrix} \quad (5)$$

where $\boldsymbol{\varepsilon}_\alpha$ is the additional strain caused by microcracking in an arbitrary spherical coordinate (r , s and t) at a certain crack density parameter noted as f . ν_m and E_m are Poisson’s and Young’s modulus of the matrix, respectively. \mathbf{s} is the crack plane traction tensor which is calculated by transforming the overall stress tensor ($\boldsymbol{\sigma}$) from global to local coordinate [59] using a stress transformation matrix (\mathbf{N}).

$$\mathbf{s} = \mathbf{N}\boldsymbol{\sigma} \quad (6)$$

Using Equation (4) for deriving the compliance matrix on a local crack plane and correlating the crack density parameters with conventional damage parameter (ω) gives local additional strain due to the microcracks as follows:

$$\boldsymbol{\varepsilon}_\alpha = \frac{\omega}{1 - \omega} \mathbf{C}_L \mathbf{s}_L \quad (7)$$

where $\mathbf{C}_L = 1/E_m \begin{bmatrix} 1 & 0 & 0 \\ 0 & 4/4 - \nu_m & 0 \\ 0 & 0 & 4/4 - \nu_m \end{bmatrix}$ is the local compliance matrix.

By applying the kinematic consistency and relating the crack density parameter to the directional damage vector $\omega(\theta, \psi)$, the overall additional strain due to all microcracking is calculated using the following equation:

$$\boldsymbol{\varepsilon}_{\text{add}} = \frac{1}{2\pi} \oint \mathbf{N}^T \mathbf{C}_L \frac{\omega}{1 - \omega} \mathbf{N} \boldsymbol{\sigma} \quad (8)$$

where \mathbf{N}_ε is strain transformation matrix.

Substituting (8) into (4) gives:

$$\boldsymbol{\sigma} = \left(\mathbf{I} + \frac{\mathbf{D}_{\text{eff}}}{2\pi} \oint \mathbf{N}^T \mathbf{C}_L \frac{\omega}{1 - \omega} \mathbf{N} \right)^{-1} \mathbf{D}_{\text{eff}} \boldsymbol{\varepsilon} \quad (9)$$

The damage evolution function can be related to the damage surface (see Equation 11), the strain at first uniaxial microcracking (ε_i) and the strain in the effectively fully microcracked condition (ε_0). Mihai and Jefferson [60] showed that for quasi-brittle materials like cementitious the following equation represents the damage evolution with reasonable accuracy:

$$\omega(\zeta) = 1 - \frac{\varepsilon_i}{\zeta} e^{-c \left(\frac{\zeta - \varepsilon_i}{\varepsilon_0 - \varepsilon_i} \right)} \quad (10)$$

where c is a constant taken to be 5.

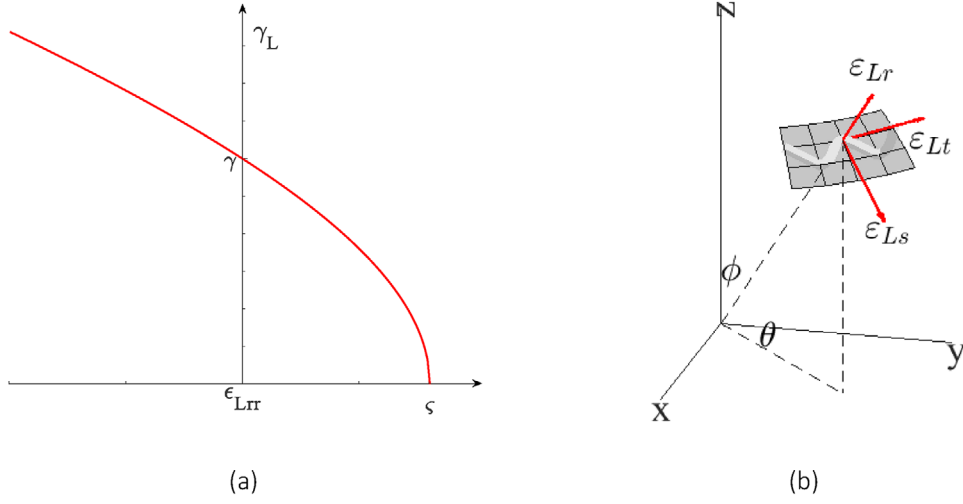


FIGURE 2 | Effective strain surface and local crack plane strain component, (a) strain surface and (b) local strain vector.

ζ is the effective strain on each crack plane, which is determined from the following damage surface equation:

$$F_{\zeta}(\boldsymbol{\varepsilon}_L, \zeta) = \left(\varepsilon_{Lrr} \left(\frac{1 + \alpha_L}{2} \right) + \sqrt{\varepsilon_{Lrr}^2 \left(\frac{1 - \alpha_L}{2} \right)^2 + r_{\zeta}^2 \gamma^2} \right) - \zeta \quad (11)$$

where $\boldsymbol{\varepsilon}_L$ is the local strain vector with three normal and shear components, $\alpha_L = \left(\frac{\nu_m}{1 - \nu_m} \right)$, $\gamma = \sqrt{\varepsilon_{Lrs}^2 + \varepsilon_{Lrt}^2}$ and $r_{\zeta} = \left(\frac{\nu_m - 1/2}{\nu_m - 1} \right)$. These functions are subjected to the standard loading/unloading conditions as follows;

$$F_{\zeta} \leq 0; \zeta \geq 0 \quad F_{\zeta} \dot{\zeta} = 0 \quad (12)$$

The damage surface as well as strain vector in local coordinate is illustrated in Figure 2.

2.3.2 | Residual Strain

The micromechanical model described in Section 2.3.1, did not consider residual strains that manifest when a damaged sample is unloaded. These residual strains are associated with residual crack displacements that occur due to mismatches in the asperities of opposing crack faces and small particles becoming lodged within the microcracks. The local crack plane relationship (see Equation 7) is modified to allow for this residual strain, as follows:

$$\mathbf{s}_L = (1 - \omega) \mathbf{D}_L \boldsymbol{\varepsilon}_L + \alpha_{\omega} \omega \mathbf{D}_L (\boldsymbol{\varepsilon}_L - \boldsymbol{\varepsilon}_{\omega}) \quad (13)$$

where $\boldsymbol{\varepsilon}_{\omega}$ is the offset strain in local coordinate at the time of unloading, and α_{ω} is a coefficient varies from 0 to 1. $\alpha_{\omega} = 0$ implies no wedging mechanism is expected during the unloading process and the unloading stiffness is the same as the damaged stiffness. This case is equivalent to the standard micromechanics (MMS) formulation illustrated in Figure 3c. When $\alpha_{\omega} = 1$, the unloading stiffness is equal to the initial elastic stiffness and the residual strain is maximised.

By following the same procedure explained earlier, the constitutive equation considering the residual displacement may be derived as follows:

$$\boldsymbol{\sigma} = \left(\mathbf{I} + \frac{\mathbf{D}_{\text{eff}}}{2\pi} \oint \mathbf{N}_{\varepsilon}^T [[(1 - \omega) + \alpha_{\omega} \omega] - 1]^{-1} \mathbf{C}_L \mathbf{N} \right)^{-1} \mathbf{D}_{\text{eff}} \left(\boldsymbol{\varepsilon} - \frac{I}{2\pi} \oint \mathbf{N}_{\varepsilon}^T [(1 - \omega) + \alpha_{\omega} \omega]^{-1} \alpha_{\omega} \omega \boldsymbol{\varepsilon}_{\omega} \right) \quad (14)$$

Table 1 shows the numerical implementation algorithm of the proposed equations.

Figure 3 illustrates the loading and unloading behaviour derived from the proposed formulation. This figure compares the responses from the MMS formulation with the enhanced micromechanics formulation to capture the residual strain (micromechanical methods residual strain, MMR) effect with $\alpha_{\omega} = 1$.

2.4 | Autogenous Healing Formulation

Davies and Jefferson [61] presented a micromechanical model for simulating microcracking and instantaneous healing. This model has been updated in the present work to include (i) time-dependent healing, (ii) to allow for residual microcrack closing strain and (iii) to strictly comply with the condition that the overall strain energy of the system should not change due to healing alone.

The healing process can commence under any loading conditions (loading or unloading) once some damage has occurred. The wedging potential also commences with damage. In addition, the amount of healing at a specific time depends on the level of the damage and the healing rate.

The following constitutive equation on a local crack plane accounts for all of the aforementioned mechanisms.

$$\mathbf{s}_L = (1 - \omega) \mathbf{D}_L \boldsymbol{\varepsilon}_L + \alpha_{\omega} ((\omega - h_v) \mathbf{D}_L (\boldsymbol{\varepsilon}_L - \boldsymbol{\varepsilon}_{\omega}) + h_v \omega_h \mathbf{D}_{Lh} (\boldsymbol{\varepsilon}_L - \boldsymbol{\varepsilon}_{\omega} - \boldsymbol{\varepsilon}_h)) + h_v \mathbf{D}_{Lh} (1 - \omega_h) (\boldsymbol{\varepsilon}_L - \boldsymbol{\varepsilon}_h) \quad (15)$$

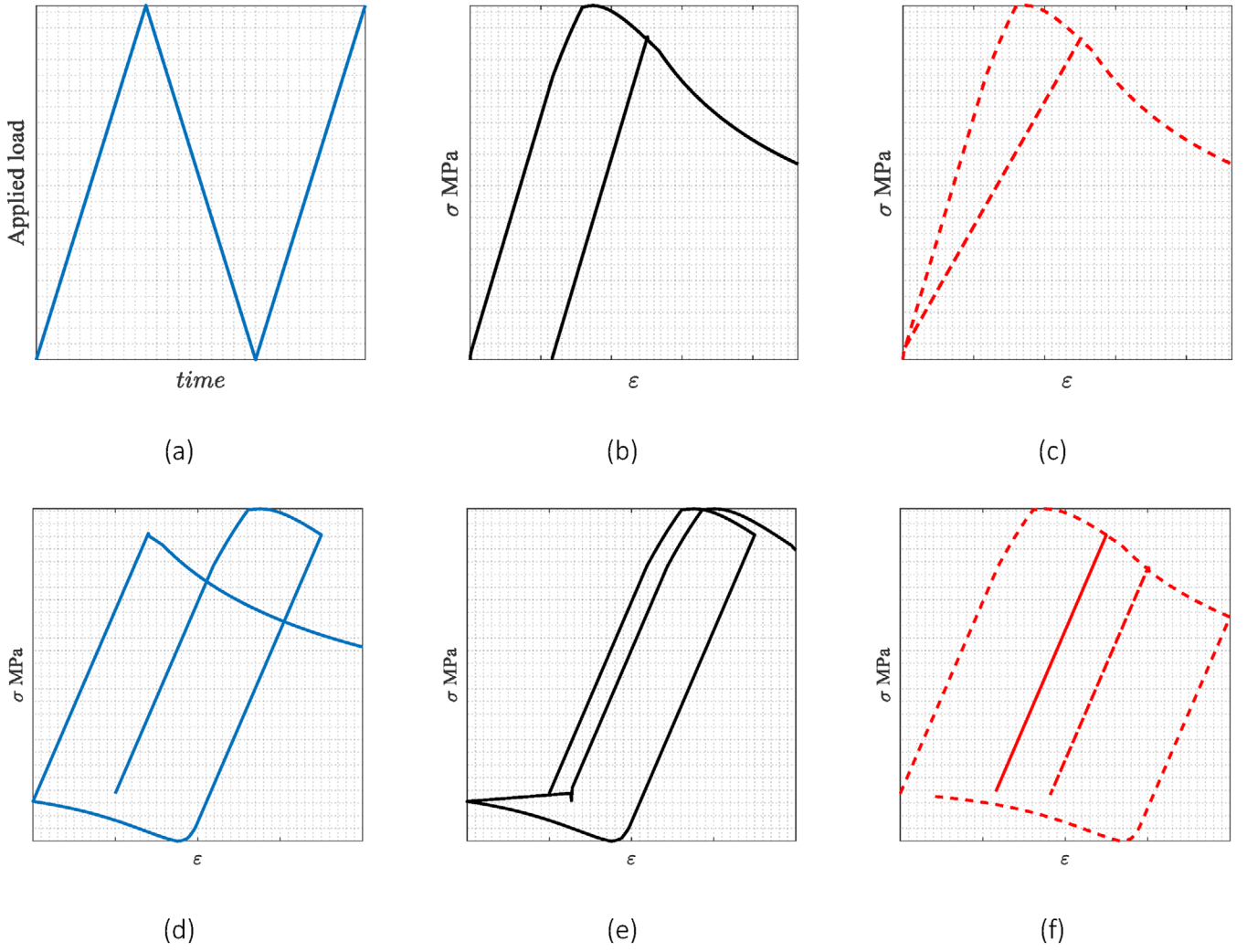


FIGURE 3 | Constitutive behaviour, (a) loading unloading path, (b) behaviour with permanent strain, (c) without residual strain, (d) cyclic behaviour with tensile wedging, (e) cyclic behaviour without wedging in tension and (f) multiple loading unloading.

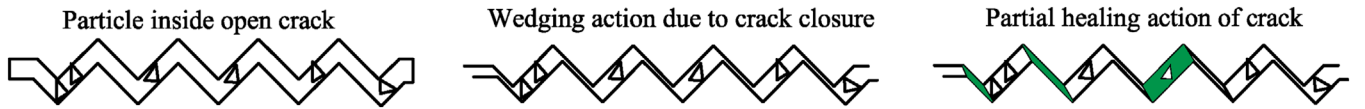


FIGURE 4 | Illustration of the cracking, wedging and healing processes.

where h_v represents the amount of healed material. This parameter varies from 0 to ω at a specific time based on the healing rate. ϵ_h is the healing strain vector. This is derived through satisfying stress-free conditions during the healing step where there should be no changes in stress tensor before and after the healing process. ω_h is the damage parameter of healed material. This superposition process is illustrated in Figure 4 schematically.

Applying the same method, the overall secant stiffness considering the wedging and healing process is calculated as follows:

$$\mathbf{D}_{\text{sech}} = \left(\mathbf{I} + \frac{\mathbf{D}_{\text{eff}}}{2\pi} \oint \mathbf{N}_\epsilon^T [\mathbf{D}_{wh}^{-1} - \mathbf{C}_L] \mathbf{N} \right)^{-1} \mathbf{D}_{\text{eff}} \quad (16)$$

where \mathbf{D}_{wh} is the wedging healing compliance in the local coordinate system.

$$\mathbf{D}_{wh} = (1 - \omega) \mathbf{D}_L + \alpha_\omega (\omega - h_v) \mathbf{D}_L + \alpha_\omega h_v \omega_h \mathbf{D}_{Lh} + h_v (1 - \omega_h) \mathbf{D}_{Lh} \quad (17)$$

The global offset strain caused by the healing and wedging process is given by:

$$\epsilon_{Gh} = \frac{\mathbf{I}}{2\pi} \oint \mathbf{N}_\epsilon^L \mathbf{A}^{-1} (h_v (1 - \omega_h) \mathbf{D}_{Lh}) \epsilon_h \quad (18)$$

For a single-cycle healing event with and without the wedging strain phenomenon is illustrated in Figure 5. The stiffness and strength recovery difference in these two mechanisms

TABLE 1 | Micromechanical model algorithm.

<i>Inpt:</i> $\alpha_\omega, \zeta_{pr}, \sigma_0, \Delta\varepsilon, \Delta\sigma$	Enter, required input parameters	
(Mechanical and damage evolution properties)		
Loading phase		
1:	for $i = 1$ to n_i	Loop over integration directions
2:	$\varepsilon_{L_i} = \mathbf{N}_{\varepsilon_i} \varepsilon$	Calculate local strain in each direction
3:	$\zeta(\varepsilon_{L_i}) = \frac{\varepsilon_{L_{rr}}}{2} \left[1 + \left(\frac{\mu}{q} \right)^2 \right] + \frac{1}{2q^2} \left(\sqrt{(q^2 - \mu^2)^2 \varepsilon_{L_{rr}}^2 + 4q^2 \gamma_L^2} \right)$	Find the effective strain parameters
4:	$\zeta(\varepsilon_{L_i}) = \max(\zeta_{pr}(\varepsilon_{L_i}), \zeta(\varepsilon_{L_i}))$	Update the maximum effective strain parameters
5:	Update $\omega_i, \omega(\zeta_i) = 1 - \frac{\varepsilon_i}{\varepsilon_0} e^{-c \left(\frac{\zeta - \varepsilon_i}{\varepsilon_0 - \varepsilon_i} \right)}$	Update damage parameters
6:	end	
7:	$\sigma = \left(\mathbf{I} + \frac{\mathbf{D}_{eff}}{2\pi} \sum_{i=1}^{29} \mathbf{N}_{\varepsilon_i}^T \frac{\omega_i}{1 - \omega_i} \mathbf{C}_L \mathbf{N}_i \right)^{-1} \mathbf{D}_{eff} \varepsilon$	Find secant stiffness and stress tensor for the microcracked material using an iterative procedure,
8:	if Unloading phase	If in an unloading phase
9:	$\omega_{pr} \leftarrow \omega$	Store the latest damage parameter in loading stage
10:	for $i = 1$ to n_i	Loop over each crack plane direction
11:	$A_i = (1 - \omega_i) + \alpha_\omega \omega_i$	Store the damage parameters
12:	end	
13:	$\mathbf{D}_{sec} = \left(\mathbf{I} + \frac{\mathbf{D}_{eff}}{2\pi} \sum_{i=1}^{29} \mathbf{N}_{\varepsilon_i}^T [A_i^{-1} - 1] \mathbf{C}_L \mathbf{N}_i w_i \right)^{-1} : \mathbf{D}_{eff}$	Update secant stiffness
14:	$\varepsilon_{G\omega} = \varepsilon - \mathbf{D}_{sec}^{-1} \sigma_{pr}$	Find the global offset residual strain
15:	$\sigma = \mathbf{D}_{sec} (\varepsilon - \varepsilon_{G\omega})$	Calculate the stress
16:	end	

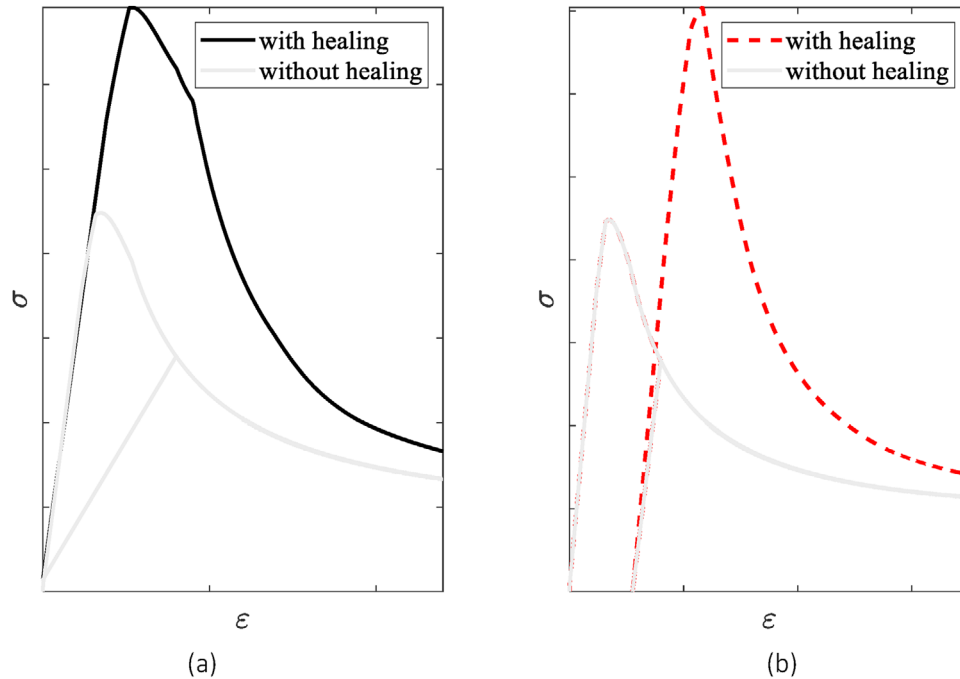


FIGURE 5 | Constitutive behaviour of self-healing lime, (a) without residual strain and (b) with residual strain.

TABLE 2 | Synopsis of the experimental programme and sampling process.

	Sample Designation	Age (days)	Level of damage	Healing period (days)	Considered for the model calibration	Considered for validation
Group_1	In_age_14W_14W	14	0%	14	✓	—
	In_age_14W_28W			28	✓	—
	In_age_28W_14W	28		14	—	—
	In_age_28W_28W			28	—	—
	In_age_56W_14W	56		14	—	—
	In_age_56W_28W			28	—	—
	In_age_84W_14W	84		14	✓	—
	In_age_84W_28W			28	✓	—
Group_2	Pr_age_14W_14W	14	70% Pre-peak	14	✓	—
	Pr_age_14W_28W			28	✓	—
	Po_age_14W_14W		90% Post-peak	14	✓	✓
	Po_age_14W_28W			28	✓	✓
	Pr_age_28W_14	28	70% Pre-peak	14	—	✓
	Pr_age_28W_28W			28	—	✓
	Po_age_28W_14W		90% Post-peak	14	—	—
	Po_age_28W_28W			28	—	—
	Pr_age_56W_14W	56	70% Pre-peak	14	—	—
	Pr_age_56W_28W			28	—	—
	Po_age_56W_14W		90% Post-peak	14	—	✓
	Po_age_56W_28W			28	—	✓
	Pr_age_84W_14W	84	70% Pre-peak	14	✓	✓
	Pr_age_84W_28W			28	✓	✓
	Po_age_84W_14W		90% Post-peak	14	✓	—
	Po_age_84W_28W			28	✓	—

indicates the importance of considering the exact physical process happening during material loading history.

3 | Experimental Materials and Methods

The experimental programme focusses on the mechanical behaviour of lime-based samples, monotonically tested in compression. Cube specimens were precracked at different ages (14–84 days) and up to different levels of damage (70% of the compression strength in the pre-peak regime; 90% of the compression strength in the post-peak regime), and then cured in water for between 14 and 28 days. More details on the experimental arrangement and healing efficiencies in terms of compressive strength and ultrasonic pulse velocity can be found in [11].

3.1 | Mortar Mix and Curing Procedure

The mix design produced mortars consistent with those used in retrofitting and restoration work [62, 63]. The mix constituents and proportions of the mortar comprised: NHL 5 (299 kg/m³); calcium hydroxide Ca(OH)₂(299 kg/m³); 0–2 mm dried dolomite sand (896 kg/m³); and water (66 kg/m³). The same mix proportions, constituents and mixing protocol were used to form all lime-based mortar specimens. The dry components,

namely NHL5, Ca(OH)₂ and sand, were initially mixed for a duration of 2–5 min. At this stage, a small quantity of water was added and mixed for an additional 5 min until the mixture achieved a stiff consistency. Subsequently, the remaining water was added and mixed for an additional 5 min. Specimens were made in the laboratory in cubes of 50 mm × 50 mm × 50 mm using polycarbonate moulds, the moulds were filled in three layers, with the initial 20 mm thick layer. All specimens were demoulded after 96 h, stored in room temperature at 23 ± 2°C and 50% ± 4% RH and tested at 14–84 days.

3.2 | Experimental Arrangement

The cubic lime-based mortar samples were monotonically tested under uniaxial compression using Galdabini Sun 20 testing machine and at a displacement ratio equal to 0.2 mm/min.

The experimental programme, as presented in Table 2, is separated into two main groups. The aim of Group_1 was to evaluate the compressive strength of undamaged samples at different ages (14–84 days) subjected to further hydration for 14–28 days by complete immersion in water. Based on the results obtained in Group_1, the Group_2 samples were predamaged to 70% of the compression strengths in the pre-peak regime and 90% of the compressive strength in the post-peak regime, as represented in

TABLE 3 | Microstructure mechanical properties.

Phase/properties	Volume fraction (%)	E (N/mm ²)	ν	f_t (N/mm ²)	ε_0	ε_{lv}
Matrix	25	1.309×10^3	0.3	0.24	0.00457	0.00018
Aggregate	75	1.54752×10^{-3}	0.05	—	—	—

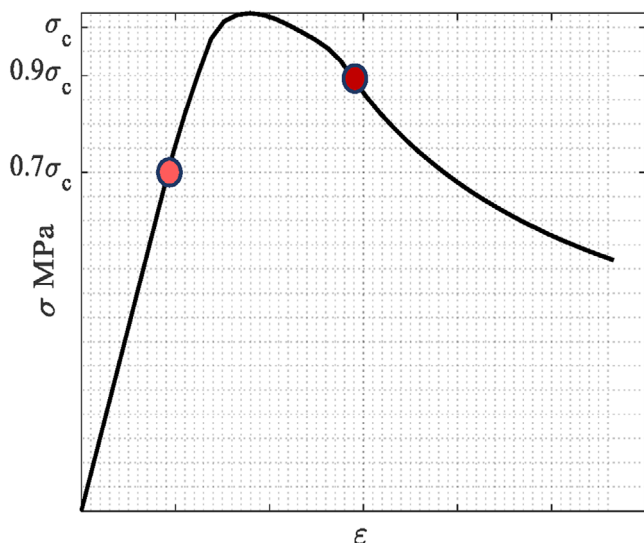


FIGURE 6 | Loading–unloading points.

Figure 6. After the predamage stage, samples were placed in water for 14–28 days. Each step of the experimental program involved casting three samples.

The lime mortar as well as its constituent phases properties are noted in Table 3, these values are used as input parameters for the micromechanics model. Firstly, the model’s ability to capture the residual strain during the unloading process is tested for the sample under undamaged condition.

4 | Model Response

This section focusses on the calibration of the self-healing micromechanical model that was introduced in the previous section. To provide context, this section begins with an examination of existing constitutive models for the uniaxial compressive behaviour of concrete. The applicability of these uniaxial models to lime mortars is considered, along with their limitations. The section continues with a description of the calibration and validation of the self-healing micromechanical model. Lastly, the section presents some investigations conducted to ascertain the model’s capacity to simulate damage-healing cycles.

The self-healing micromechanical model, presented in the previous section, has been implemented in a Mathcad (2020) sheet using a constitutive driver algorithm. The wedging process is also introduced to this formulation to account for the residual strain at each unloading phase. The model follows a specified path, which is defined by stress and/or strain increments (i.e. σ and ε , respectively) [61]. The simulation considers the period

of time before healing occurs (t_0 to t_h), the moment of healing commences (t_h) as well as the posthealing phase (t_h to t_{end}).

4.1 | Model Calibration

Several constitutive models for the uniaxial compressive behaviour of concrete have been discussed in the literature but these do not explicitly address the behaviour of lime-based mortars. Firstly, various models such Saenz [50], Desay and Krishnan [49], Carreira and Chu [52], Popovics [51] and Fib model code [53] have been examined and compared with data from lime mortar experiments. Each of these models follows a parametric approach characterised by parameters that hold physical significance, namely: (i) the maximum stress, usually representing the concrete strength measure; (ii) the strain corresponding to the maximum stress; (iii) the modulus of elasticity; (iv) the secant modulus at the yield point and (v) the ultimate strain which defines the point of failure. Figure 7 illustrates the comparison between the experimental data and the models mentioned earlier. Among those Carrera and Chu model has demonstrated to fit a wide spectrum of experimental data remarkably well.

Secondly, the conventional micromechanics model (as described in Section 2.3.1) was calibrated using a limited number of mechanical parameters such as f_t and E . The results from the micromechanical model were then compared with the experimental stress–strain response for the entire data set, showing an excellent correlation. An example can be seen in Figure 8a,b. The mechanical properties derived at different material ages were used to assess the changes in the effective strain parameters. This allowed for the evaluation of the undamaged component of the lime mortar over time.

Moreover, within the context of developing the new micromechanical model for representing lime-based mortars, the empirical approach employed in the Carrera and Chu model was compared to both the experimental data and the response predicted by the new model. The comparison allowed the assessment of the performance of the newly developed model and validated in accurately predicting the behaviour of lime-based mortars, as shown in Figure 8b.

The comparison allowed the performance of the newly developed model to be assessed and also showed that it can accurately predict the behaviour of lime-based mortars.

As can be seen in Figure 8a, the proposed micromechanical model is able to capture the loading and unloading responses accurately. In particular, the model is also capable of representing residual strains (Figure 8b), which allows it to simulate the mechanical behaviour of lime-based mortars under cyclic loading.

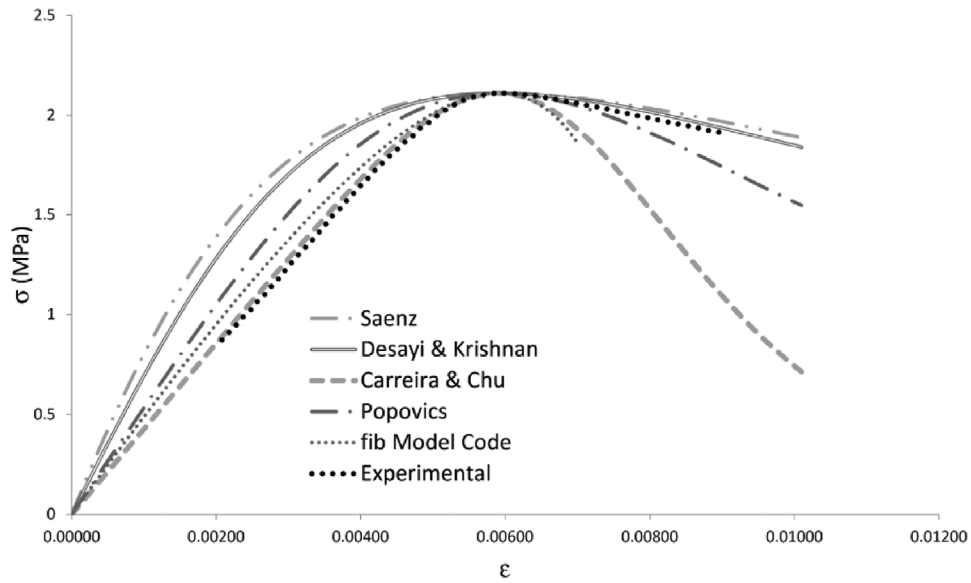


FIGURE 7 | Example fit of main models to the experimental data.

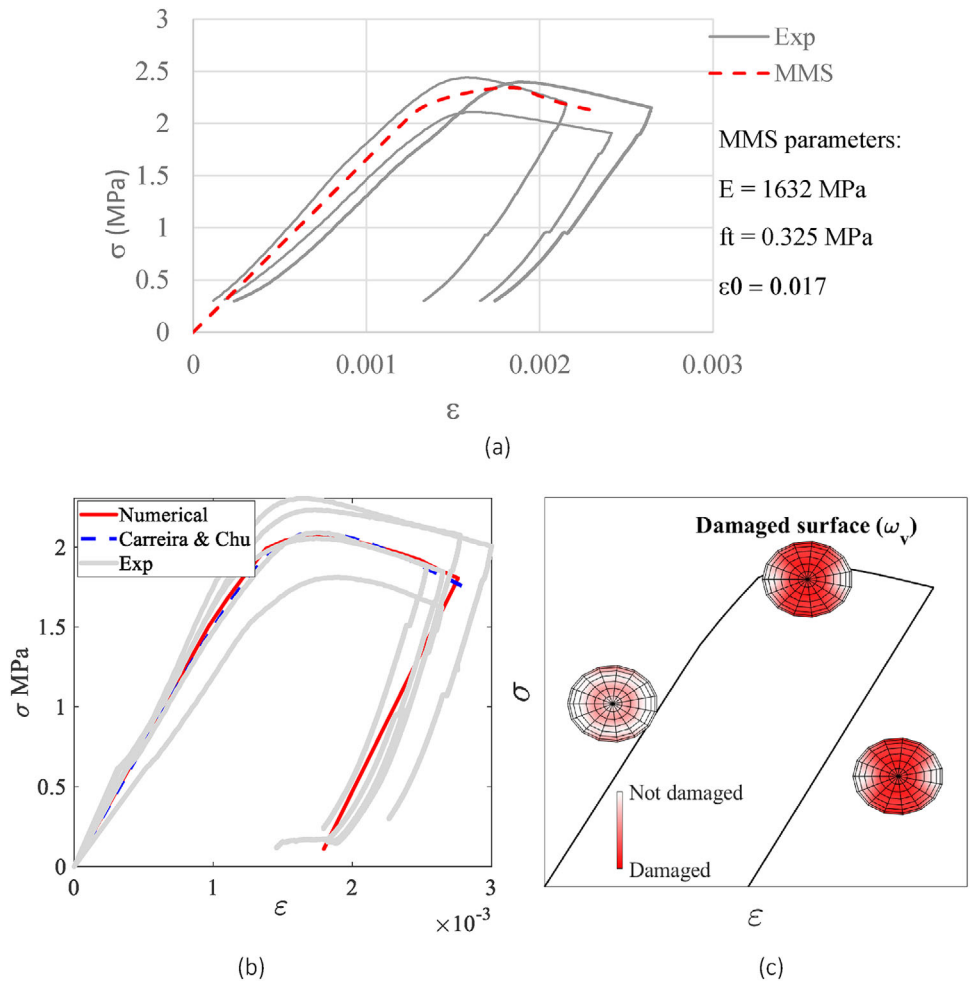


FIGURE 8 | Loading unloading curve for damage phase, (a) standard micromechanics (MMS) model calibration, (b) MMR model validation and (c) damage evolution.

TABLE 4 | Material input parameter.

Sample/properties	E (N/mm ²)	f_t (N/mm ²)	E_h (N/mm ²)	ν_h	f_{th} (N/mm ²)	ε_{lvh}	ε_{oh}
Po-14-14W-28W	1.488×10^3	0.24	1.1785×10^3	0.3	0.30	0.00025	0.00457
Po-14-28W-28W	1.488×10^3	0.24	1.1785×10^3	0.3	0.37	0.00032	0.00457
Po-56-14W-28W	1.206×10^3	0.18	955.72	0.3	0.18	0.00019	0.00457
Po-56-28W-28W	1.206×10^3	0.18	955.72	0.3	0.26	0.00027	0.00457

For the model calibration, the data from samples in undamaged and damaged conditions - either in the pre-peak or in the post-peak regime - tested at 14 and 84 days were used. These samples were subject to different curing periods, during which healing occurred. For the model calibration, only the data from one cycle healing were used (see Table 2). Also, after the model parameters were calibrated, the other data which are for different sample ages and level of the damage were used for the model validation with respect to both monotonic and cyclic loading behaviour.

The single-cycle healing responses of the samples used for the model calibration are illustrated in Figure 9, key model parameters are summarised in Table 4.

According to the experimental results, the healing efficiency strongly depends on sample age, level of the damage and curing time.

Using the extracted data from all responses, a healing efficiency curve, as a function of age and curing time, is calculated. Figure 10 shows the prediction parameters derived from the experimental data. These functions were used for informing the healing efficiency parameters used in the proposed model. Based on the expected level of the damage and curing time, the model can estimate the response of the sample after the static healing period.

Numerical simulations are performed on samples under the damage-healing cycle, considering the higher level of damage, up to 90% in the post-peak regime. The input parameters for these self-healing scenarios are noted in Table 4. In this table, the subscript h is showing the parameters for healing materials.

The numerical simulation shows that the model can predict the strength and stiffness recovery of the lime material after the autogenous healing process as a function of age, level of the damage and curing time. Figure 11 shows the comparison between experiments and numerical simulations for the samples noted in Table 4.

For a closer look at the damage and healing evolution parameters, the directionally dependent damage and healing parameters for the Po-14W-14W case are presented in Figure 12. The amount of healing of the original material as well as the re-damaging phase can be calculated. For this uniaxial compressive test, the healing was initiated in a fully unloading condition at a strain of 0.0017 and the second healing cycle was activated at a strain of 0.00475. Figure 11a,b shows that in the second healing cycle, the model can capture the healing process due to both damage of

the original materials, as indicated by an increase in h_v , as well as the re-healing of the previously damaged-healed material by the reduction in ω_h .

Numerical simulation of the experiment with the pre-peak conditions (Figure 13) shows that less mechanical regain occurred compared to the experimental results. Since the source of the healing in this micromechanical formulation is the damage of the original material, the model is unable to capture mechanical regain due to further hydration of unhydrated virgin materials, which is the main reason for the stiffness and strength rises in pre-peak conditions (See Figure 13).

It is important to note that the limitations of the self-healing micromechanical model likely arise from the variables considered in the experimental tests, such as age, level of damage, condition and healing time, which might not fully capture the variability observed in real-world conditions. Moreover, the limited number of tests on mechanical parameters means that the model parameters are calibrated with a degree of uncertainty. Currently, the model does not account for variations in the chemical composition of different lime mortars, which can influence their healing capabilities. However, the current model provides a valuable foundation for understanding self-healing mechanisms and future iterations will aim to incorporate these factors to enhance its accuracy and reliability.

5 | Conclusions and Final Remarks

Masonry structures are crucial assets to our built heritage since they represent historical craftsmanship, cultural identity and architectural legacy, providing essential insights into past construction methods and societal evolution. Given their important role for economies and societies, the assessment, preventive conservation and maintenance of historical masonry structures remain key focusses of political strategy in both the UK and Europe. It is widely acknowledged that preventive measures are far more cost-effective than spending on damage repair. Damage to historic structures often results in the loss of both buildings and artworks, leading to: (i) a tangible loss of artistic and historical materials, and (ii) an intangible loss of memory and cultural identity for the people to whom that legacy belongs. It is widely acknowledged that preventive measures are far more cost-effective than spending on damage repair.

The analysis of historic masonry structures is complex due to limited resources for studying their mechanical behaviour, including non-destructive testing, laboratory testing and developing

Condition

14 days samples

84 days samples

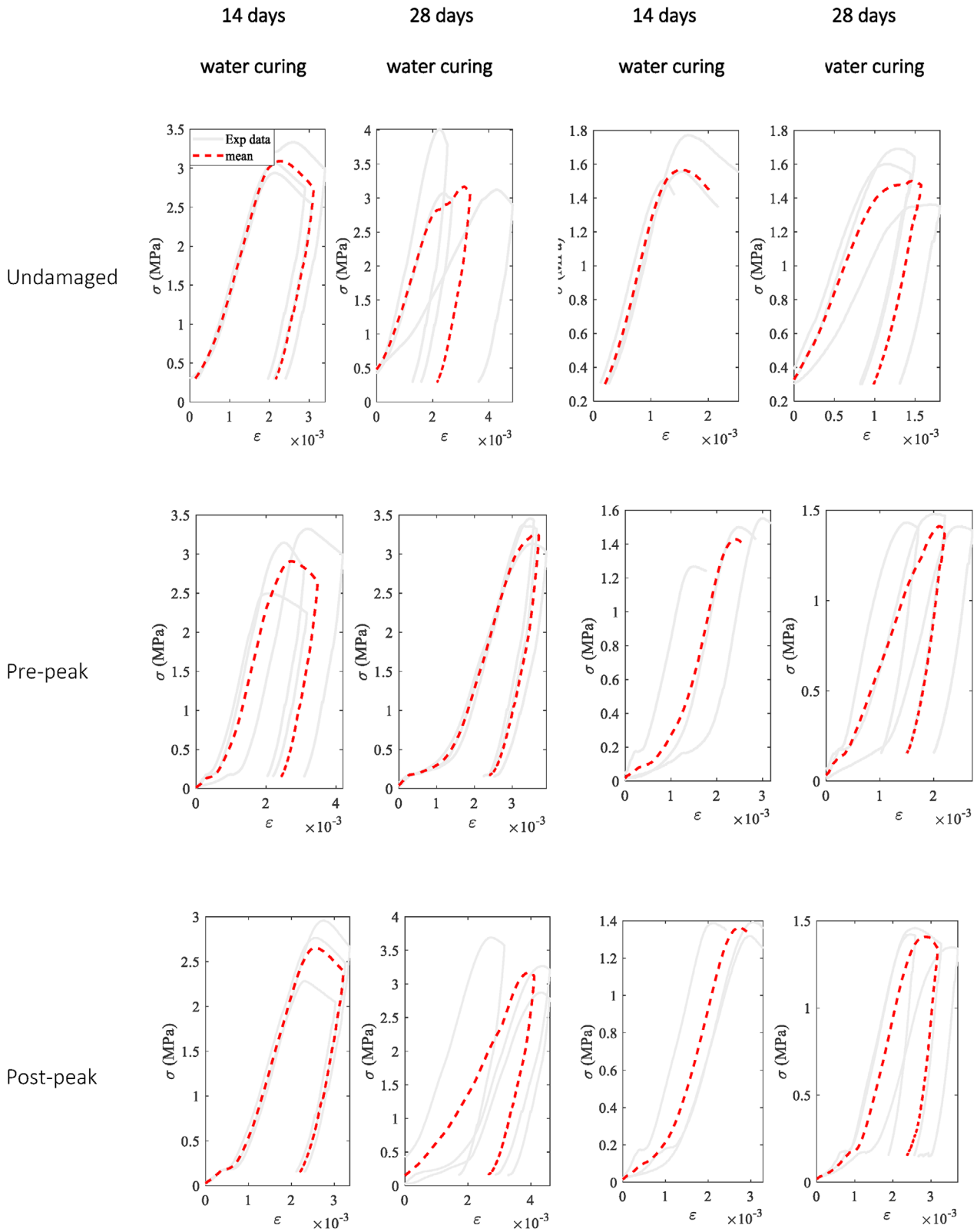


FIGURE 9 | Stress–strain graphs for experimental data (Exp. Data) used for validation.

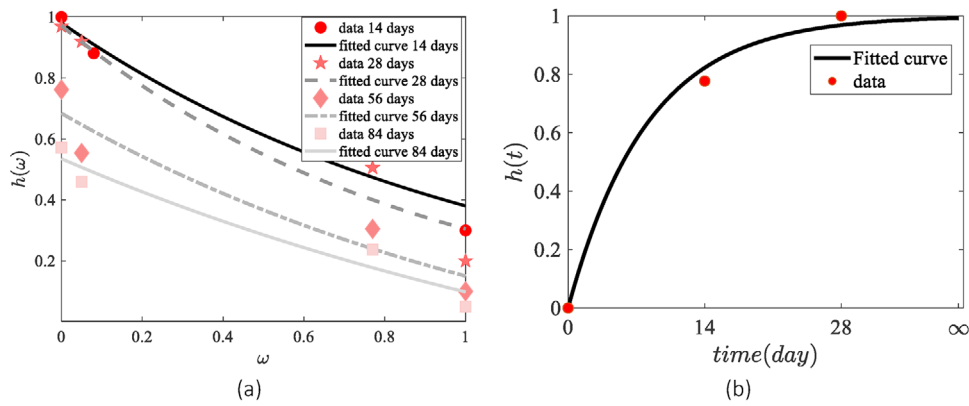


FIGURE 10 | Calibrated functions for healing efficiency, (a) healing relation to the damage level and (b) healing relation to the curing time.

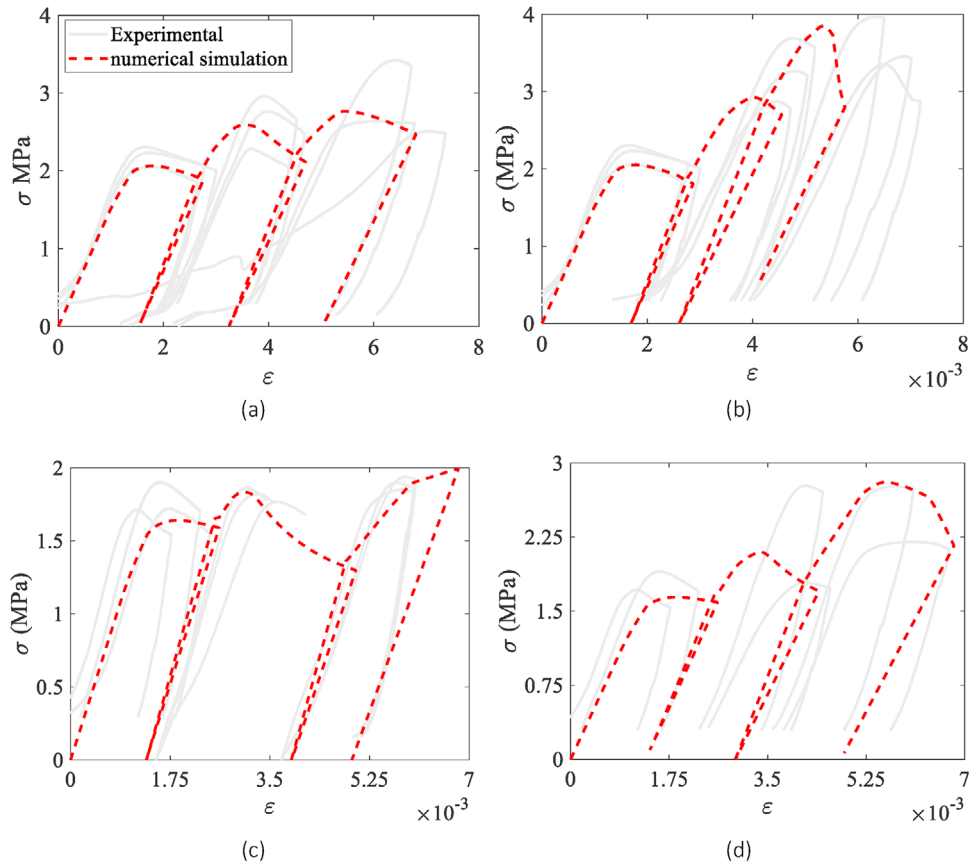


FIGURE 11 | For two cycles healing scenarios responses for where healing happened after 90% post-peak capacity (Po samples). (a) 14-14W-28W, (b) 14-28W-28W, (c) 56-14W-28W and (d) 56-28W-28W.

reliable numerical tools. Additionally, the inherent challenges in applying existing knowledge further complicate the analysis of these structures.

The finite element method (FEM) and discrete element method (DEM) require precise knowledge of the fundamental behaviour of materials as crucial inputs. One significant challenge is the difficult and costly characterisation of the mechanical properties of the materials used. Detailed material characterisation under diverse loads and environmental conditions, along with understanding their evolution over time, is crucial for governmental

decisions regarding load values and partial safety factors for materials.

Architectural heritage, including historical buildings and monuments, often employs lime mortar masonry that can develop microcracks over time. Lime-based mortars possess autogenous healing capabilities, where atmospheric water dissolves lime, and upon evaporation, deposits it to heal cracks.

Existing literature on lime mortar properties is limited compared with that on cement mortar and considerably less modelling

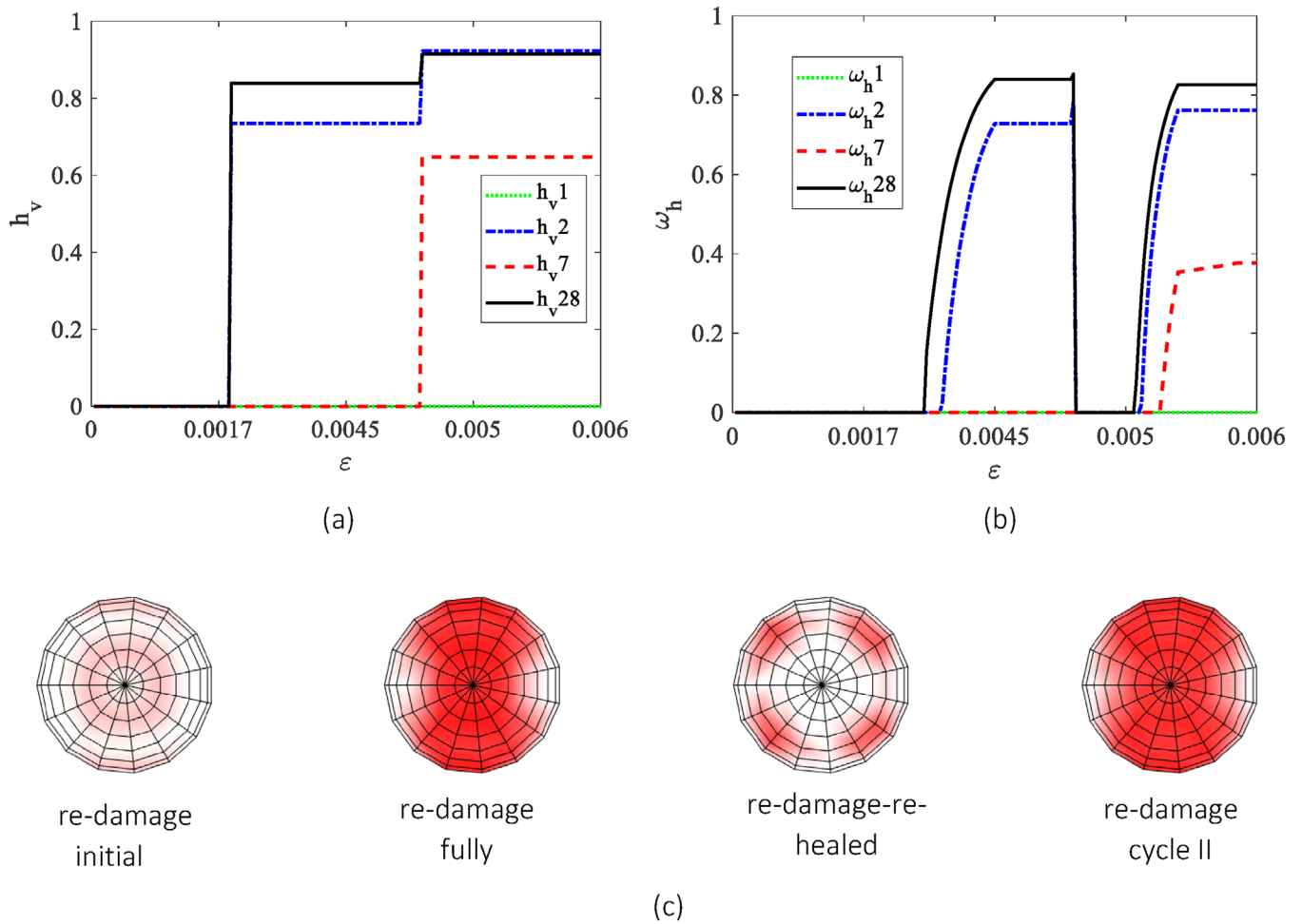


FIGURE 12 | Damage and healing evolution parameters, (a) healing parameter, (b) re-damage parameter and (c) re-damage evolution phase.

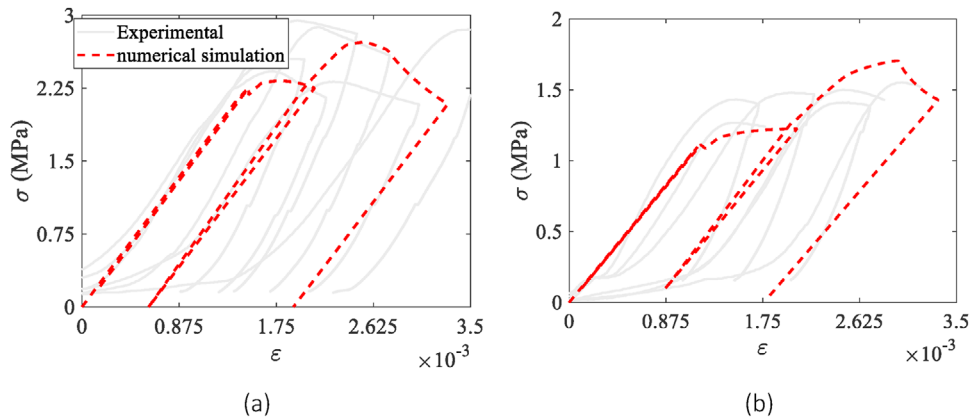


FIGURE 13 | Pre-peak condition, (a) sample age 28 days and (b) sample age 84 days.

work has been undertaken on this material than its cement counterpart. Computational tools are crucial for assessing structural behaviour and self-healing processes in masonry components. The paper proposes a micromechanical model for simulating cracking and healing in lime-based mortars.

The existing two-phase composite micromechanical constitutive model, originally designed for simulating concrete, considers

anisotropic microcracking. This serves as a natural foundation for the further development of a model specifically tailored to the autogenous healing behaviour of lime-based mortars. The model was calibrated using experimental data on the mechanical performance of NHL samples under compression. Cube specimens were precracked at different ages and levels of damage, and then cured in water for specific periods to evaluate the autogenous healing efficacy.

The model parameters were adjusted and fine-tuned based on the results obtained from one healing cycle. Subsequently, the model's accuracy and reliability were assessed by validating it against additional data. Based on the findings of this study, the following conclusions are made:

- lime-based mortars demonstrate remarkable autogenous self-healing capabilities. The effectiveness of self-healing is influenced by the extent of damage and the age at which the damage occurred. These mortars have the ability to undergo multiple cycles of healing, that is up to three cycles, with higher healing potential observed in less damaged specimens relative to those precracked at earlier ages.
- some lime samples exhibited a greater unloading slope compared to the initial loading phase, indicating that material compaction during compression increases Young's modulus during unloading.
- the proposed micromechanical model accurately captures the loading and unloading responses of lime-based mortars, including residual strains. Notably, the level of damage was found to be the key factor influencing the magnitude of residual strain for lime-based materials. Furthermore, this residual strain's origin is intrinsically linked to the degree of damage incurred.
- the model is able to simulate the damage-healing cyclic behaviour of lime mortar specimens with good accuracy. Numerical simulations demonstrate the model's ability to predict strength and stiffness recovery after autogenous healing.

Both numerical modelling and experimental testing consistently demonstrated that as the level of damage and the age of the sample increased, the effectiveness of autonomous healing in lime-based mortars diminished. These findings strongly suggest the necessity of incorporating supplementary self-healing additives to enhance the long-term self-healing performance of lime-based mortars.

The proposed model paves the way for implementing the micromechanical model in masonry finite element analyses, providing a comprehensive understanding of historical masonry structures with low computational cost. Integrating self-healing behaviour in historic masonry structure modelling allows for more accurate performance prediction, providing realistic assessments of how structures will perform over time, especially under various loading and environmental conditions. It also enables the optimisation of repair technologies, leading to innovative solutions that enhance durability and longevity. Additionally, this approach facilitates better maintenance scheduling by focussing on critical areas and potentially reducing the frequency of interventions.

Moreover, with respect to modern masonry structures, this will empower engineers and architects to make informed decisions during the design phase, ensuring that structures can withstand the test of time and diverse loads. This approach aligns with the imperative need to minimise resource consumption and environmental impact, contributing to the design of more durable and resilient structures.

Author Contributions

Cristina De Nardi: conceptualisation, methodology, writing—original draft, writing—review and editing, project administration, funding acquisition. **Sina Sayadi:** conceptualisation, methodology, writing—original draft and editing. **Iulia Mihai:** supervision. **Anthony Jefferson:** conceptualisation, methodology, writing—review and editing, supervision, project administration, funding acquisition.

Acknowledgements

This research was funded by the Leverhulme Trust ECF-2022-235 and Engineering and Physical Sciences Research Council (EPSRC), grant number EP/P02081X/1. This research was funded also by the European Union's Horizon 2020 research and innovation program under the Marie Skłodowska-Curie grant agreement no. 860006; SMARTINCS Project. This work was also supported by an STSM Grant from the COST Action CA15202. The authors would also like to acknowledge the considerable help and expertise of Robert Davies.

Conflicts of Interest

The authors declare no conflicts of interest.

Data Availability Statement

The data that support the findings of this study are available from the corresponding author upon reasonable request.

References

1. M. Harlov-Csörtán, *Heritage and the City*, eds. R. Kusek and J. Purchla (Krakow, 2017), 315p, <https://doi.org/10.18030/socio.hu.2018en.118>.
2. K. F. Abdulla, L. S. Cunningham, and M. Gillie, "Simulating Masonry Wall Behaviour Using a Simplified Micro-Model Approach," *Engineering Structures* 151 (2017): 349–365, <https://doi.org/10.1016/j.engstruct.2017.08.021>.
3. A. Arizzi and G. Cultrone, "The Influence of Aggregate Texture, Morphology and Grading on the Carbonation of Non-Hydraulic (aerial) Lime-Based Mortars," *Quarterly Journal of Engineering Geology and Hydrogeology* 46, no. 4 (2013): 507–520, <https://doi.org/10.1144/qjgeh2012-017>.
4. R. Lawton, D. Fujiwara, A. Szydłowska, et al., *Heritage and the Value of Place* (London: Simetrica–Jacobs, 2021).
5. European Commission, "EU Policy for Cultural Heritage," accessed July 17, 2024, <https://culture.ec.europa.eu/cultural-heritage/eu-policy-for-cultural-heritage>.
6. National Institute of Building Sciences, "Climate Adaptation, Mitigation and Resiliency," (2023), accessed July 17, 2024, <https://www.nibs.org/about/climate-adaptation>.
7. I. Papayianni, "The Longevity of Old Mortars," *Applied Physics A* 83, no. 4 (2006): 685–688, <https://doi.org/10.1007/s00339-006-3523-2>.
8. F. O. Anderegg, "Autogeneous Healing in Mortars Containing Lime," *ASTM Bulletin* no. 16 (1942): 22.
9. B. Lubelli, T. G. Nijland, and R. P. J. Van Hees, "Simulation of Self-Healing of Dolomitic Lime Mortar" in *Proceedings of 13th Euroseminar on Microscopy Applied to Building Materials* (Ljubljana, Slovenia, June 14–18, 2011).
10. B. Lubelli, T. G. Nijland, and R. P. J. Van Hees, "Self-Healing of Lime Based Mortars: Microscopy Observations on Case Studies," *Heron* 56, no. 1 (2011): 75–92.
11. C. De Nardi, A. Cecchi, L. Ferrara, A. Benedetti, and D. Cristofori, "Effect of Age and Level of Damage on the Autogenous Healing of Lime Mortars," *Composites Part B Engineering* 124 (2017): 144–157, <https://doi.org/10.1016/j.compositesb.2017.05.041>.

12. L. Binda, C. Tedeschi, and G. Baronio, "Mechanical Behaviour at Different Ages, of Masonry Prisms With Thick Mortar Joints Reproducing a Byzantine Masonry," (paper presentation, Proceedings of the 8th North American Masonry Conference, Austin, Texas, June 6–9, 1999).
13. V. Sarhosis, S. W. Garrity, and Y. Sheng, "Influence of Brick–Mortar Interface on the Mechanical Behaviour of Low Bond Strength Masonry Brickwork Lintels," *Engineering Structures* 88 (2015): 1–11, <https://doi.org/10.1016/j.engstruct.2014.12.014>.
14. C. Groot, R. Veiga, I. Papayianni, et al., "RILEM TC 277-LHS Report: Lime-Based Mortars for Restoration – A Review on Long-Term Durability Aspects and Experience From Practice," *Materials and Structures* 55, no. 10 (2022), <https://doi.org/10.1617/s11527-022-02052-1>.
15. T. P. Tassios, "Meccanica delle Murature," (Liguori Editore, Napoli, 1988), 240.
16. R. Grazzini, G. Misseri, and L. Rovero, "A Bi-Modulus Material Model for Bending Test on NHL3.5 Lime Mortar," *Materials* 16, no. 2 (2023): 486, <https://doi.org/10.3390/ma16020486>.
17. C. Diogo and P. Figueiredo, *Properties and Performance of Lime Mortars for Conservation: The Role of Binder Chemistry and Curing Regime* (Bath: University of Bath, 2018).
18. L. Binda, G. Baronio, and C. Tedeschi, "Experimental Study on the Mechanical Role of Thick Mortar Joints in Reproduced Byzantine Masonry," in *International RILEM Workshop on Historic Mortars: Characteristics and Tests, Paisley, Scotland, May 12–14, 1999* (2000), 227–247, <https://masonrymagazine.com/Default?pageID=8128>.
19. P. B. Lourenço, "Computations on Historic Masonry Structures," *Progress in Structural Engineering and Materials* 4, no. 3 (2002): 301–319, <https://doi.org/10.1002/pse.120>.
20. P. B. Lourenço, "Analysis and Restoration of Ancient Masonry Structures: Guidelines and Examples," in *Proceedings of IMTCR-04 Innovative Materials and Technologies for Construction and Restoration* (Lecce, 2004), vol. 4, 1–15.
21. C. De Nardi, A. Cecchi, and L. Ferrara, "The Influence of Self-Healing Capacity of Lime Mortars on the Behaviour of Brick-Mortar Masonry Subassemblies," *Key Engineering Materials* 747 (2017): 465–471, <https://doi.org/10.4028/www.scientific.net/KEM.747.465>.
22. C. De Nardi, A. Cecchi, and L. Ferrara, "Assessing the Influence of Self-Healing Capacity of Lime-Based Mortars on Brick-Mortar Interface Strength in Masonry Units," in *MATEC Web of Conferences* (Bologna, Italy: EDP Sciences, 2018), <https://doi.org/10.1051/mateconf/201819902015>.
23. P. B. Lourenço and J. Pina-Henriques, "Validation of Analytical and Continuum Numerical Methods for Estimating the Compressive Strength of Masonry," *Computers and Structures* 84, no. 29 (2006): 1977–1989, <https://doi.org/10.1016/j.compstruc.2006.08.009>.
24. E. Donval, D. T. Pham, G. Hassen, P. de Buhan, and M. Vigroux, "3D analytical and Numerical Upper-Bound Homogenization Approaches to the in-Plane Strength Domain of a Running-Bond Masonry Wall," *International Journal for Numerical and Analytical Methods in Geomechanics* 47, no. 10 (2023): 1742–1771, <https://doi.org/10.1002/nag.3537>.
25. P. B. Lourenço, *Computational Strategies for Masonry Structures* (The Netherlands: Delft University Press, 1996).
26. R. Kamai and Y. H. Hatzor, "Numerical Analysis of Block Stone Displacements in Ancient Masonry Structures: A New Method to Estimate Historic Ground Motions," *International Journal for Numerical and Analytical Methods in Geomechanics* 32, no. 11 (2008): 1321–1340, <https://doi.org/10.1002/nag.671>.
27. L. Nguyen-Tuan, C. Könke, V. Bettzieche, and T. Lahmer, "Damage Identification Using Inverse Analysis in Coupled Thermo-Hydro-Mechanical Problems Applied to Masonry Dams," *International Journal for Numerical and Analytical Methods in Geomechanics* 42, no. 2 (2018): 256–273, <https://doi.org/10.1002/nag.2723>.
28. P. Roca, M. Cervera, G. Gariup, and L. Pela', "Structural Analysis of Masonry Historical Constructions. Classical and Advanced Approaches," *Archives of Computational Methods in Engineering* 17, no. 3 (2010): 299–325, <https://doi.org/10.1007/s11831-010-9046-1>.
29. S. Stoyanov, P. Mason, and C. Bailey, "Smearred Shell Modelling Approach for Structural Analysis of Heritage Composite Structures – An Application to the Cutty Sark Conservation," *Computers and Structures* 88, no. 11 (2010): 649–663, <https://doi.org/10.1016/j.compstruc.2010.02.005>.
30. J. G. Rots, "Numerical Simulation of Cracking in Structural Masonry," *Heron* 36, no. 2 (1991): 49–63, <https://www.scopus.com/inward/record.uri?eid=2-s2.0-0026367868&partnerID=40&md5=ffc0876b708e05aa4d8f780b68656b46>.
31. P. B. Lourenço, "Computational Strategies for Masonry Structures: Multi-Scale Modelling, Dynamics, Engineering Applications and Other Challenges," in *Congreso De Métodos Numéricos En Ingeniería* (2013), <http://www.isise.net>.
32. E. Sacco, "Micro, Multiscale and Macro Models for Masonry Structures," in *Mechanics of Masonry Structures*, ed. M. Angelillo (Vienna: Springer Vienna, 2014): 241–291, https://doi.org/10.1007/978-3-7091-1774-3_6.
33. J. M. Adam, A. Brencich, T. G. Hughes, and T. Jefferson, "Micromodelling of Eccentrically Loaded Brickwork: Study of Masonry Wallettes," *Engineering Structures* 32, no. 5 (2010): 1244–1251, <https://doi.org/10.1016/j.engstruct.2009.12.050>.
34. A. Gabor, E. Ferrier, E. Jacquelin, and P. Hamelin, "Analysis and Modelling of the in-Plane Shear Behaviour of Hollow Brick Masonry Panels," *Construction & Building Materials* 20, no. 5 (2006): 308–321, <https://doi.org/10.1016/j.conbuildmat.2005.01.032>.
35. Ł. Kowalewski and M. Gajewski, "Determination of Failure Modes in Brick Walls Using Cohesive Elements Approach," *Procedia Engineering* 111 (2015): 454–461, <https://doi.org/10.1016/j.proeng.2015.07.116>.
36. A. A. Akbarzade and A. A. Tasnimi, "Nonlinear Analysis and Modeling of Unreinforced Masonry Shear Walls Based on Plastic Damage Model," *JSEE* 11, no. 4 (2010).
37. A. Spada, G. Giambanco, and P. Rizzo, "Damage and Plasticity at the Interfaces in Composite Materials and Structures," *Computer Methods in Applied Mechanics and Engineering* 198, no. 49 (2009): 3884–3901, <https://doi.org/10.1016/j.cma.2009.08.024>.
38. K. M. Dolatshahi and A. J. Aref, "Two-Dimensional Computational Framework of Meso-Scale Rigid and Line Interface Elements for Masonry Structures," *Engineering Structures* 33, no. 12 (2011): 3657–3667, <https://doi.org/10.1016/j.engstruct.2011.07.030>.
39. A. Rahman and T. Ueda, "Experimental Investigation and Numerical Modeling of Peak Shear Stress of Brick Masonry Mortar Joint Under Compression," *Journal of Materials in Civil Engineering* 26, no. 9 (2014), [https://doi.org/10.1061/\(asce\)mt.1943-5533.0000958](https://doi.org/10.1061/(asce)mt.1943-5533.0000958).
40. L. Pelà, M. Cervera, and P. Roca, "Continuum Damage Model for Orthotropic Materials: Application to Masonry," *Computer Methods in Applied Mechanics and Engineering* 200, no. 9 (2011): 917–930, <https://doi.org/10.1016/j.cma.2010.11.010>.
41. A. Penna, S. Lagomarsino, and A. Galasco, "A Nonlinear Macroelement Model for the Seismic Analysis of Masonry Buildings," *Earthquake Engineering and Structural Dynamics* 43, no. 2 (2014): 159–179, <https://doi.org/10.1002/eqe.2335>.
42. T. Janaraj and M. Dhanasekar, "Finite Element Analysis of the in-Plane Shear Behaviour of Masonry Panels Confined With Reinforced Grouted Cores," *Construction & Building Materials* 65 (2014): 495–506, <https://doi.org/10.1016/j.conbuildmat.2014.04.133>.
43. P. Lourenço and J. G. Rots, "On the Use of Homogenisation Techniques for the Analysis of Masonry Structures," *Masonry International* 11, no. 1 (1997): 26–32.

44. S. Sayadi, E. Ricketts, E. Schlangen, P. Cleall, I. Mihai, and A. Jefferson, "Effect of Microstructure Heterogeneity Shapes on Constitutive Behaviour of Encapsulated Self-Healing Cementitious Materials," *MATEC Web of Conferences* 378 (2023): 09004, <https://doi.org/10.1051/mateconf/202337809004>.
45. A. Costigan, S. Pavia, and O. Kinnane, "An Experimental Evaluation of Prediction Models for the Mechanical Behavior of Unreinforced, Lime-Mortar Masonry Under Compression," *Journal of Building Engineering* 4 (2015): 283–294, <https://doi.org/10.1016/j.jobbe.2015.10.001>.
46. M. Valluzzi, N. Mazzon, M. Munari, F. Casarin, and C. Modena, "Effectiveness of Injections Evaluated by Sonic Tests on Reduced Scale Multi-Leaf Masonry Building Subjected to Seismic Actions," NDTCE'09, Non-Destructive Testing in Civil Engineering (Nantes, France, June 30–July 3, 2009).
47. R. Davies and A. Jefferson, "Micromechanical Modelling of Self-Healing Cementitious Materials," *International Journal of Solids and Structures* 113-114 (2017): 180–191, <https://doi.org/10.1016/j.ijsolstr.2017.02.008>.
48. A. D. Jefferson and T. Bennett, "Micro-Mechanical Damage and Rough Crack Closure in Cementitious Composite Materials," *International Journal for Numerical and Analytical Methods in Geomechanics* 31, no. 2 (2007): 133–146, <https://doi.org/10.1002/nag.551>.
49. P. Desayi and S. Krishnan, "Equation for the Stress-Strain Curve of Concrete," *ACI Journal* 61, no. 3, (1964): 345–350.
50. L. Saenz, "Discussion of Equation for the Stress-Strain Curve of Concrete, by Desayi and Krishnan," *ACI Journal Proceeding* 61, no. 6 (1964): 1129–1235.
51. S. Popovics, "A Review of Stress-Strain Relationships for Concrete," *ACI Journal Proceedings* 67, no. 3 (1970): 243–248, <https://doi.org/10.14359/7266>.
52. D. J. Carreira and K.-H. Chu, "Stress-Strain Relationship for Plain Concrete in Compression," *ACI Journal* 82, no. 72 (1985): 797–804.
53. J. Walraven and A. B. Vliet, *Fib Model Code for Concrete Structures 2010* (The Netherlands: Ernst & Sohn, 2010).
54. J. D. Eshelby and R. E. Peierls, "The Determination of the Elastic Field of an Ellipsoidal Inclusion, and Related Problems," *Proceedings of the Royal Society of London. Series A, Mathematical and Physical Sciences* 241, no. 1226 (1997): 376–396, <https://doi.org/10.1098/rspa.1957.0133>.
55. T. Mori and K. Tanaka, "Average Stress in Matrix and Average Elastic Energy of Materials With Misfitting Inclusions," *Acta Metallurgica* 21, no. 5 (1973): 571–574, [https://doi.org/10.1016/0001-6160\(73\)90064-3](https://doi.org/10.1016/0001-6160(73)90064-3).
56. H. Christian and M. Herbert, "Shotcrete Elasticity Revisited in the Framework of Continuum Micromechanics: From Submicron to Meter Level," *Journal of Materials in Civil Engineering* 17, no. 3 (2005): 246–256, [https://doi.org/10.1061/\(ASCE\)0899-1561\(2005\)17:3\(246\)](https://doi.org/10.1061/(ASCE)0899-1561(2005)17:3(246)).
57. A. D. Jefferson and T. Bennett, "Micro-Mechanical Damage and Rough Crack Closure in Cementitious Composite Materials," *International Journal for Numerical and Analytical Methods in Geomechanics* 31, no. 2 (2007): 133–146, <https://doi.org/10.1002/nag.551>.
58. B. Budiansky and R. J. O'connell, "Elastic Moduli of a Cracked Solid," *International Journal of Solids and Structures* 12, no. 2 (1976): 81–97, [https://doi.org/10.1016/0020-7683\(76\)90044-5](https://doi.org/10.1016/0020-7683(76)90044-5).
59. A. D. Jefferson, "Craft—A Plastic-Damage-Contact Model for Concrete. II. Model Implementation With Implicit Return-Mapping Algorithm and Consistent Tangent Matrix," *International Journal of Solids and Structures* 40, no. 22 (2003): 6001–6022, [https://doi.org/10.1016/S0020-7683\(03\)00391-3](https://doi.org/10.1016/S0020-7683(03)00391-3).
60. I. C. Mihai and A. D. Jefferson, "A Material Model for Cementitious Composite Materials With an Exterior Point Eshelby Microcrack Initiation Criterion," *International Journal of Solids and Structures* 48, no. 24 (2011): 3312–3325, <https://doi.org/10.1016/j.ijsolstr.2011.08.001>.
61. R. Davies and A. Jefferson, "Micromechanical Modelling of Self-Healing Cementitious Materials," *International Journal of Solids and Structures* 113-114 (2017): 180–191, <https://doi.org/10.1016/j.ijsolstr.2017.02.008>.
62. F. E. Penas, "Hydraulic Lime Mortars for Wall Rendering," (PhD Thesis, Instituto Superior Tecnico, Universidade tecnica de Lisboa, 2008).
63. B. A. Silva, A. P. Ferreira Pinto, and A. Gomes, "Influence of Natural Hydraulic Lime Content on the Properties of Aerial Lime-Based Mortars," *Construction & Building Materials* 72 (2014): 208–218, <https://doi.org/10.1016/J.CONBUILDMAT.2014.09.010>.